AGU PUBLICATIONS

JGR

Journal of Geophysical Research: Solid Earth

RESEARCH ARTICLE
10.1002/2015JB012512

# Rupture complexity and the supershear transition on rough faults

**Lucile Bruhat[1], Zijun Fang[2], and Eric M. Dunham[1,3]**

[1]Department of Geophysics, Stanford University, Stanford, California, USA, [2]ConocoPhillips Company, Houston, Texas, USA, [3]Institute of Computational and Mathematical Engineering, Stanford University, Stanford, California, USA

**Key Points:**
- Roughness favors diverse rupture styles, including supershear transitions
- Supershear is observed even at low background shear stress (outside the Burridge-Andrews range)
- The high sensitivity and nonlinearity of the rupture style call for statistical descriptions

**Supporting Information:**
- Table S1

**Correspondence to:**
L. Bruhat,
lbruhat@stanford.edu

**Citation:**
Bruhat, L., Z. Fang, and E. M. Dunham (2016), Rupture complexity and the supershear transition on rough faults, *J. Geophys. Res. Solid Earth*, *121*, 210–224, doi:10.1002/2015JB012512.

Received 10 SEP 2015
Accepted 25 DEC 2015
Accepted article online 5 JAN 2016
Published online 23 JAN 2016



**Abstract** Field investigations suggest that supershear earthquakes occur on geometrically simple, smooth fault segments. In contrast, dynamic rupture simulations show how heterogeneity of stress, strength, and fault geometry can trigger supershear transitions, as well as other complex rupture styles. Here we examine the Fang and Dunham (2013) ensemble of 2-D plane strain dynamic ruptures on fractally rough faults subject to strongly rate weakening friction laws to document the effect of fault roughness and prestress on rupture behavior. Roughness gives rise to extremely diverse rupture styles, such as rupture arrests, secondary slip pulses that rerupture previously slipped fault sections, and supershear transitions. Even when the prestress is below the Burridge-Andrews threshold for supershear on planar faults with uniform stress and strength conditions, supershear transitions are observed. A statistical analysis of the rupture velocity distribution reveals that supershear transients become increasingly likely at higher stress levels and on rougher faults. We examine individual ruptures and identify recurrent patterns for the supershear transition. While some transitions occur on fault segments that are favorably oriented in the background stress field, other transitions happen at the initiation of or after propagation through an unfavorable bend. We conclude that supershear transients are indeed favored by geometric complexity. In contrast, sustained supershear propagation is most common on segments that are locally smoother than average. Because rupture style is so sensitive to both background stress and small-scale details of the fault geometry, it seems unlikely that field maps of fault traces will provide reliable deterministic predictions of supershear propagation on specific fault segments.

## 1. Introduction

Often idealized as single planes, natural faults actually show slight deviations from planarity at all scales [*Brown and Scholz*, 1985; *Power et al.*, 1988; *Power and Tullis*, 1991, 1995; *Lee and Bruhn*, 1996; *Sagy and Brodsky*, 2009; *Candela et al.*, 2009, 2012]. On a rough fault, the local stresses are perturbed during rupture growth, leading to rapid accelerations and decelerations of the rupture front, slip heterogeneity, resistance to slip, and inelastic deformation [*Chester and Chester*, 2000; *Dieterich and Smith*, 2009; *Dunham et al.*, 2011a, 2011b; *Fang and Dunham*, 2013; *Shi and Day*, 2013]. Furthermore, numerous studies provide compelling evidence that fault slip is spatially and temporally variable [*Heaton*, 1982; *Beroza and Spudich*, 1988; *Wald and Somerville*, 1995; *Meng et al.*, 2011]. Most of the complexities observed in earthquake source parameters can then be ascribed to irregularities in the fault geometry [*Andrews*, 1980]. The rupture variability also generates energetic high-frequency waves [*Haskell*, 1964; *Spudich and Frazer*, 1984; *Dunham et al.*, 2011b; *Shi and Day*, 2013] that are of particular interest to earthquake engineers, who need accurate constraints on high-frequency ground motion when modeling building response.

In this study, we explore the effect of fault roughness and background shear stress on rupture behavior. Our work examines 2-D plane strain dynamic ruptures on band-limited fractally rough faults subject to strongly rate weakening friction laws as described in *Dunham et al.* [2011a, 2011b]. Through the analysis of over a thousand dynamic ruptures on different realizations of self-similar faults compiled in *Fang and Dunham* [2013], we demonstrate that fault roughness can explain the wide diversity in rupture styles observed in nature, such as reverse ruptures, coexistence of secondary and even multiple slip pulses, and supershear transitions.

The possibility for an earthquake rupture to propagate at velocities exceeding the *S* wave speed, also called supershear rupture, has been known since the 1970s [*Burridge*, 1973; *Andrews*, 1976; *Das and Aki*, 1977].

Both theoretical and numerical models were developed at that time, demonstrating that mode II ruptures could propagate faster than the *S* wave speed and up to the *P* wave speed. In particular, on planar faults with uniform stress and strength conditions, the ultimate speed of the rupture is determined by the nondimensional seismic *S* ratio [*Andrews*, 1976; *Das and Aki*, 1977]: $S = (\tau_p - \tau_0)/(\tau_0 - \tau_r)$, where $\tau_0$ is the background shear stress and $\tau_p$ and $\tau_r$ are the peak and residual strengths, respectively. In this study, instead of *S*, we use the nondimensional prestress $\bar{\tau}_0 = (\tau_0 - \tau_r)/(\tau_p - \tau_r) = 1/(1+S)$, as in *Kaneko and Lapusta* [2010], for instance. On homogeneously prestressed faults in 2-D, supershear transitions occur when $\bar{\tau}_0 > 0.36$ (or $S < 1.77$) [*Burridge*, 1973; *Andrews*, 1976, 1985]. For lower values of $\bar{\tau}_0$, the rupture propagates no faster than the Rayleigh wave speed. Considering a fault with given peak and residual strengths, high levels of background shear stress $\tau_0$ are then needed to transition to the supershear regime. But there is much evidence for low stress levels on many faults.

For example, earthquakes occur as self-healing slip pulses [*Heaton*, 1990]. Slip pulses arise naturally on faults with strongly rate weakening friction [*Tsutsumi and Shimamoto*, 1997; *Tullis and Goldsby*, 2003; *Di Toro et al.*, 2004] at sufficiently low background shear stress [*Zheng and Rice*, 1998]. At higher shear stress, ruptures take the form of expanding cracks that have an order of magnitude more slip per rupture length than observed [*Noda et al.*, 2009]. On planar faults with off-fault plasticity, *Dunham et al.* [2011a] showed that self-sustaining pulses occur when the ratio of shear to effective normal stress $\tau_0/\sigma_0$ is approximately 0.25. The critical stress level required for rupture propagation does increase with fault roughness [*Fang and Dunham*, 2013], and it is possible that this increased background stress makes supershear more likely. However, we demonstrate here that supershear ruptures are likely to occur at stresses well below the Burridge-Andrews threshold and that fault geometric complexity plays a central role in initiating the supershear transition.

Supershear ruptures have been inferred for a number of large earthquakes, most of them associated with strike-slip faults, such as the 1979 Imperial Valley earthquake [*Archuleta*, 1984], the 1999 Izmit earthquake [*Ellsworth and Celebi*, 1999; *Bouchon et al.*, 2000, 2001], the 2001 Kunlun (Tibet) earthquake [*Bouchon and Vallée*, 2003; *Robinson et al.*, 2006; *Vallée et al.*, 2008], the 2002 Denali (Alaska) earthquake [*Aagaard and Heaton*, 2004; *Dunham and Archuleta*, 2004; *Ellsworth et al.*, 2004], and the 2013 Craig (Alaska) earthquake [*Yue et al.*, 2013]. Over the last decade, field investigations on documented supershear earthquakes have led to the idea that fault geometry is directly linked to the likelihood of ruptures propagating at supershear speeds [*Bouchon et al.*, 2010]. Observations suggest that the fault segment where a rupture propagates at a supershear speed is linear and narrow. Considering a planar segment in a constant regional stress field, the local stresses should be uniform. This implies that supershear speeds are associated with simple fault geometry, and consequently homogeneous stress and strength conditions. However, several numerical simulation studies [*Dunham et al.*, 2003; *Dunham*, 2007; *Liu and Lapusta*, 2008] demonstrated that a supershear rupture can be triggered by heterogeneity in stress and/or frictional strength and that heterogeneity is plausibly related to the fault geometry. From the observational side, when studying the 2001 Kunlun (Tibet) earthquake, *Vallée et al.* [2008] pointed out that the seismically inferred supershear transition location coincided with a local region of enhanced geometrical complexity and a change in the average strike of the fault trace.

In the present work, we study an ensemble of 2-D plane strain dynamic simulations on rough fault profiles [*Fang and Dunham*, 2013]. While most studies on fault roughness limited their analysis to a few simulations [*Dunham et al.*, 2011b; *Shi and Day*, 2013], *Fang and Dunham* [2013] simulated thousands of ruptures on 100 randomly generated self-similar fault profiles. This approach permits statistical characterization of the rupture process. The main focus of their initial work was not the description of the rupture styles induced by the roughness, but the quantification of the additional shear resistance to slip (roughness drag) to explain the high stress levels at which immature faults operate. Their work also did not distinguish supershear from sub-Rayleigh ruptures. In this study, we return to their ensemble database and document the effect of fault roughness and background shear stress on rupture style for both sub-Rayleigh and supershear ruptures. We then show that despite a very low prestress $\bar{\tau}_0$ far below the Burridge-Andrews threshold, supershear transitions are observed. By analyzing the ensemble database in a statistical manner, we demonstrate that supershear transitions are more likely on rougher faults but that sustained supershear propagation tends to occur on smoother fault segments. We also examine specific cases to identify several distinct supershear transition mechanisms and propagation behaviors associated with complex geometry.

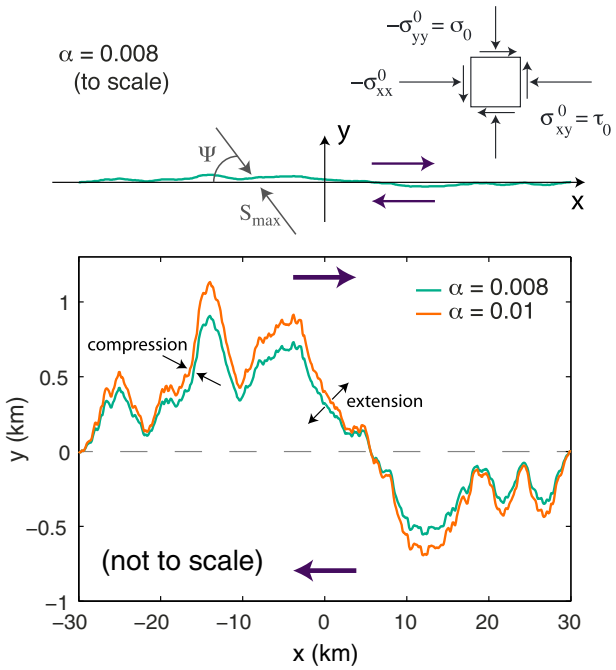


**Figure 1.** (top) Plane strain model with right-lateral slip on a band-limited self-similar fault with amplitude-to-wavelength ratio of roughness $\alpha = 0.008$. The medium is loaded with a spatially uniform stress state, with the maximum principal stress inclined at an angle $\Psi = 50°$ to the fault. (bottom) Same fault profile exaggerated in the $y$ direction for two different $\alpha$, illustrating compressional and extensional bends.

## 2. Dynamic Rupture Simulations on Rough Faults

In this section, we briefly review the approach developed by *Dunham et al.* [2011a, 2011b] and *Fang and Dunham* [2013] to build the collection of 2-D plane strain dynamic simulations on rough fault profiles. The fault is a band-limited self-similar fractal profile having root-mean-square (RMS) deviations from planarity $h_{RMS}$ proportional to the fault length $L$:

$$h_{RMS} = \alpha L, \tag{1}$$

where $\alpha$ is the amplitude-to-wavelength ratio of roughness. In the slip-parallel direction, the fault roughness is characterized by $\alpha$ between $10^{-3}$ and $10^{-2}$ [*Power and Tullis*, 1991]. Low values of roughness often indicate mature faults, suggesting that wear induced by repeated slip gradually reduces the fault roughness [*Sagy and Brodsky*, 2009; *Brodsky et al.*, 2011].

This study considers ruptures on 100 fault profiles for five values of $\alpha$ ranging from $10^{-3}$ to $10^{-2}$. The length of the fault profile is $L = 60$ km and the grid spacing is $\Delta x = 10$ m. Numerical accuracy is assured by limiting the fault roughness to wavelengths between $\lambda_{min} = 30\Delta x$ and the fault length $L$. The rough fault is then embedded in a homogeneous medium, infinite in extent. The initial stress field $\sigma^0_{ij}$ is spatially uniform, described by the background shear stress $\tau_0 = \sigma^0_{xy}$, the effective normal stress $\sigma_0 = -\sigma^0_{yy}$, and the angle $\Psi$ between the maximum principal compressive stress and the $x$ axis (Figure 1). However, because of the fault nonplanarity, the local tractions fluctuate along the fault profile. For all simulations, $\sigma_0 = 126$ MPa and $\Psi = 50°$. Our assumption of uniform stresses in the medium is certainly unrealistic, and simulations of longer-term slip evolution, involving sequences of ruptures on rough faults, are required to properly characterize stress heterogeneity and its relation to the complex fault geometry.

The simulations use a rate-and-state friction law describing evolution toward a strongly velocity weakening steady state strength. This allows a self-healing slip pulse to propagate when the background shear stress $\tau_0$ is sufficiently low [*Zheng and Rice*, 1998; *Dunham et al.*, 2011a]. Since increasing the roughness $\alpha$ increases the minimum $\tau_0$ at which self-sustaining propagation is possible [*Fang and Dunham*, 2013], $\tau_0$ varies from 35.0 MPa to 53.5 MPa (see Table S1 in the supporting information), depending on the profile roughness. In defining peak and residual strengths, $\tau_p$ and $\tau_r$, which are used to calculate $S$ and $\bar{\tau}_0$, we use the expressions in *Dunham et al.* [2011a]. In particular, the residual strength is estimated using a representative slip velocity in

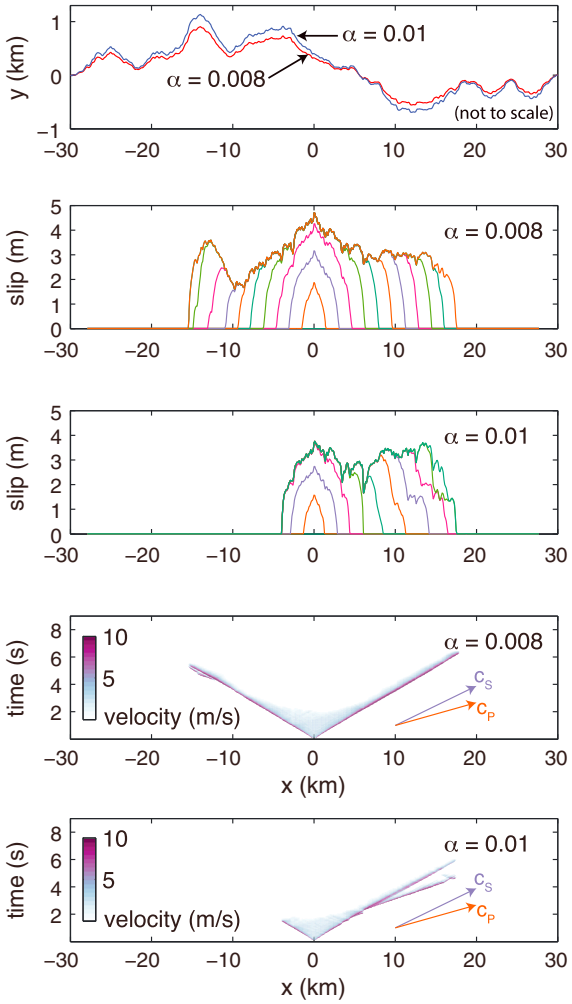


**Figure 2.** (middle) Slip every 0.56 s and (bottom) slip velocity on the same fault profile, for the same background shear stress $\tau_0 = 43.5$ MPa ($\tau_0/\sigma_0 = 0.345$ and $\bar{\tau}_0 = 0.31$), but two levels of roughness $\alpha$. Increasing roughness can both arrest the rupture and trigger a supershear transition, despite being outside the Burridge-Andrews range for supershear ($\bar{\tau}_0 > 0.36$).

the center of a crack-like rupture, rather than the fully weakened strength. *Gabriel et al.* [2012] have shown that this is essential for consistency with critical *S* or $\bar{\tau}_0$ values calculated from idealized solutions having constant $\tau_r$ within the slipping region (like self-similar crack solutions and simulations with slip-weakening friction).

The off-fault material is characterized by a noncohesive elasto-viscoplastic rheology, which prevents fault opening and unreasonably large stress concentrations at the fault complexities. Ruptures are initiated by applying a localized stress concentration at a region of high resolved shear-to-normal stress ratio. With this procedure, nucleation most often occurs within major extensional bends where the fault orientation could favor supershear transition. We discard ruptures that immediately propagate at supershear speeds to avoid bias resulting from the artificial initiation procedure. Further details on the friction, plasticity, and material parameters can be found in *Dunham et al.* [2011a, 2011b] and *Fang and Dunham* [2013]. Numerical methods, in particular, the high-order finite difference method used here, are described in *Dunham et al.* [2011a] and *Kozdon et al.* [2012, 2013].

## 3. Complexity of Rupture Style

The study of a large catalog of rupture simulations allows us to identify rupture styles that commonly emerge on rough faults. Almost all previous studies have focused solely on single, sub-Rayleigh slip pulses and cracks. Figure 2 illustrates an example of the effect of increasing roughness on rupture propagation and slip.

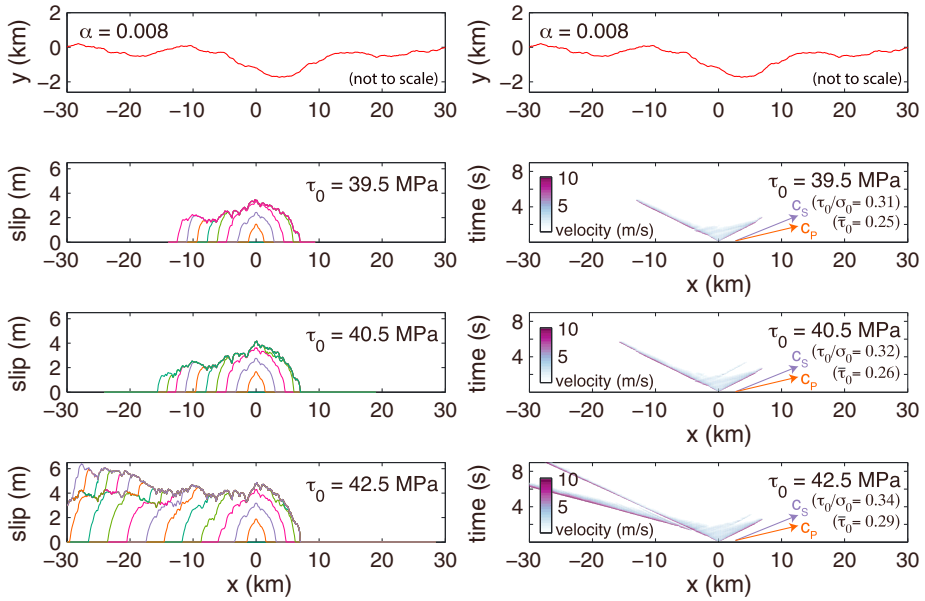


**Figure 3.** (left column) Slip every 0.56 s and (right column) slip velocity, illustrating the increase in slip heterogeneity and rupture behavior as the background shear stress $\tau_0$ is increased on the same rough fault. The fault profile (same for both columns) is shown at the top of the figure. Increasing $\tau_0$ leads to larger rupture lengths and a supershear transition.

For the lowest roughness presented here, $\alpha = 0.008$, the rupture propagates smoothly in both directions in the sub-Rayleigh regime and arrests after 5–6 s. As mentioned in *Fang and Dunham* [2013], fault roughness offers a realistic mechanism for rupture arrest. Ruptures naturally slow down and die out after encountering compressional bends, which are unfavorable to rupture propagation. Increasing the roughness slightly to $\alpha = 0.01$ dramatically alters the rupture pattern. On the left side, the rupture arrests sooner at a different compressional bend. On the other side, although the rupture propagates as far as in the previous case, a daughter crack forms at $x = 7$ km to initiate a supershear rupture; a secondary slip pulse follows, propagating at about

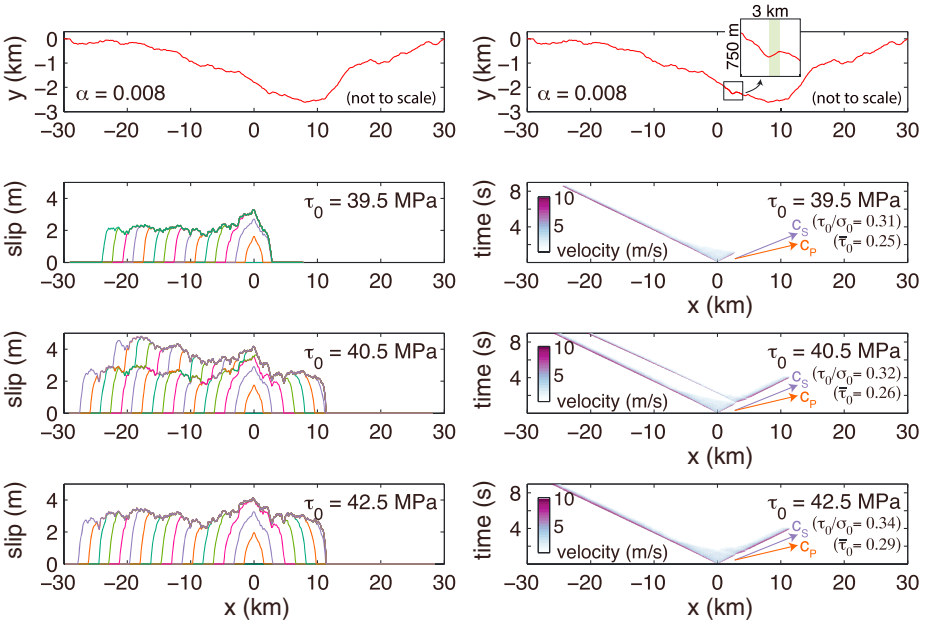


**Figure 4.** (left column) Slip every 0.56 s and (right column) slip velocity, illustrating the increase in slip heterogeneity and rupture behavior as the background shear stress $\tau_0$ is increased on the same rough fault. The fault profile (same for both columns) is shown at the top of the figure. Increasing $\tau_0$ allows a secondary rupture at the exit of a restraining bend (shown in the zoom on the right fault profile).

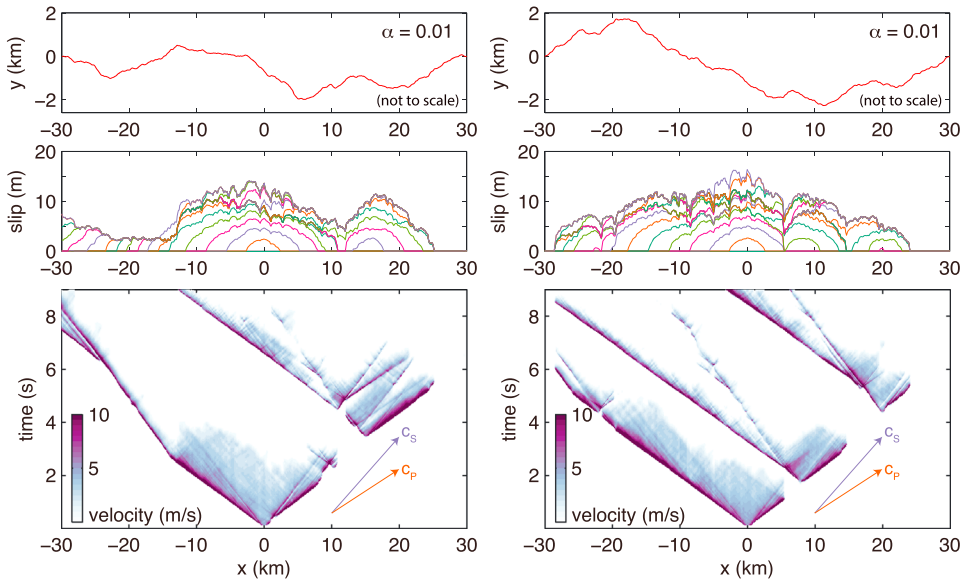


**Figure 5.** (top row) Fault profiles, (middle row) slip every 0.56 s, and (bottom row) slip velocity for two extremely complex fault ruptures. The fault roughness is $\alpha = 0.01$, and the background shear stress is $\tau_0 = 53.5$ MPa ($\tau_0/\sigma_0 = 0.42$ and $\bar{\tau}_0 = 0.46$). Large amounts of slip (>12 m) are observed close to the hypocenter in both simulations. Both ruptures start in the supershear regime, but either transition back or emit sub-Rayleigh pulses during their course.

the Rayleigh wave speed. The supershear transition is somewhat surprising, since both ruptures occur at a dimensionless background stress level of $\bar{\tau}_0 \approx 0.3$, below the $\bar{\tau}_0 > 0.36$ Burridge-Andrews range. The supershear transition initiates at a geometrical feature that is unfavorable to slip; note the local minimum in slip at this location.

The rupture process also exhibits a pronounced sensitivity to the local stress conditions, as displayed in Figures 3 and 4. Both cases show the evolution of slip and the rupture pattern on the same fault but at three different $\tau_0$. Ruptures tend to propagate farther as the background shear stress $\tau_0$ is increased, as noted by *Fang and Dunham* [2013]. In Figure 3, for $\tau_0 = 40.5$ MPa, a second slip pulse is emitted at $x = -2$ km, which then propagates for almost 10 km in the $+x$ direction. An observer near $x = 3$ km would witness the passage of two slip pulses separated by approximately 2 s. For higher levels of $\tau_0$, a supershear transition occurs at $x = -4$ km. While the local fault geometry is obviously causing the transition, the relationship between geometry and rupture speed is highly nonlinear. At lower values of background shear stress than that which triggers supershear, the rupture passes through the same geometrical feature without noticeable perturbation in rupture velocity. These examples again illustrate the onset of more complex rupture behavior but now associated with an increase in the background shear stress. As before, the supershear transition occurs at stresses ($\bar{\tau}_0 = 0.29$) well below the Burridge-Andrews threshold ($\bar{\tau}_0 = 0.36$).

Figure 4 presents an intriguing case of rerupture. The fault geometry is held fixed while the background stress is increased. At the lowest stress, the rupture stops on the right side after propagating a few kilometers. When $\tau_0$ increases (by only 1 MPa), the rupture slows down at the location of the previous arrest, but then reruptures the fault bilaterally. For even larger $\tau_0$, the abrupt cessation and resumption of rupture, which induced the secondary slip pulse, does not occur, and the rupture propagates smoothly through the region that previously disturbed it. We see here that the rupture behavior can be dramatically modified by small-scale features in the fault geometry, with the response highly dependent on the precise level of background stress.

Having a large range of roughnesses and background shear stresses at our disposal gives us the opportunity to examine rupture patterns on rough faults at higher values of $\tau_0$. These represent cases that would be uncommon but not impossible. On rough faults there is no unique threshold stress for self-sustaining propagation around which a fault would be expected to operate. Instead, faults would host ruptures over a range of stresses, in a manner that can be quantified by analysis of the ensemble database [*Fang and Dunham*, 2013]. The stress level selected here is at the high, but still plausible, range of background stresses (see Figure 8 and associated discussion later in the text). Figure 5 presents examples of these cases on two different

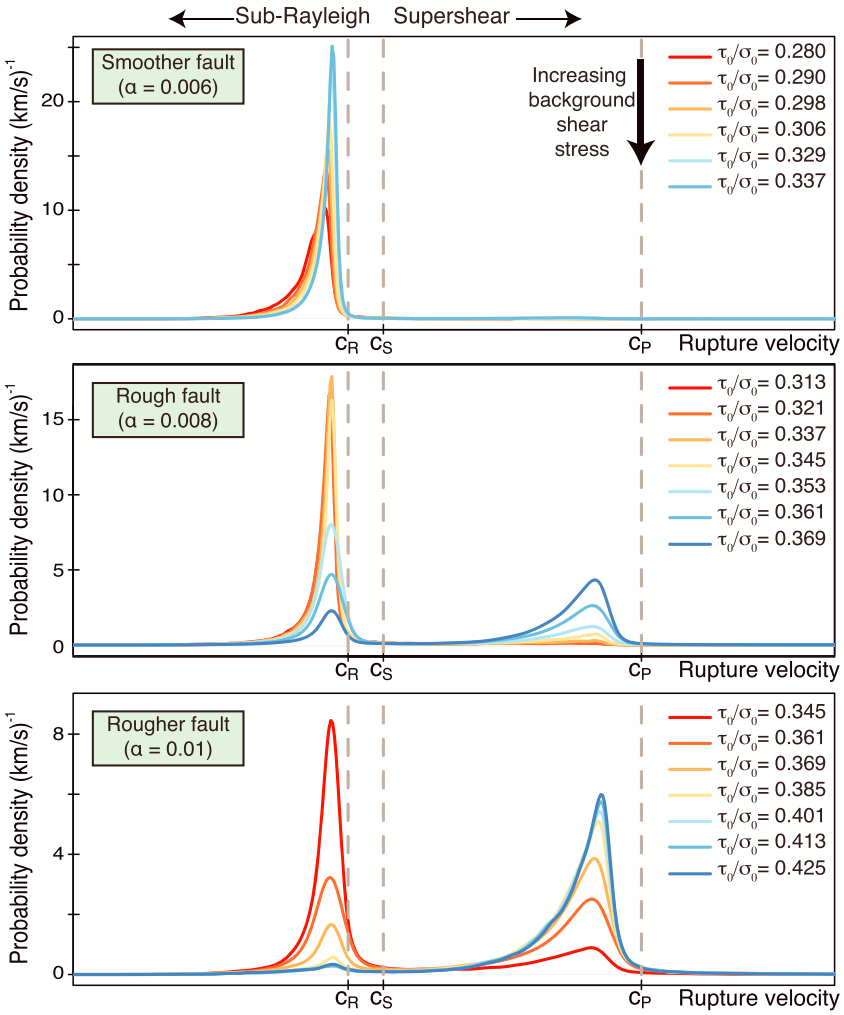


**Figure 6.** Distributions of rupture velocity for all simulations, classified in order of increasing roughness $\alpha$ and background shear stress $\tau_0$. $c_R$ is the Rayleigh wave speed, $c_S$ is the $S$ wave speed, and $c_P$ is the $P$ wave speed. (top) On a smooth fault ($\alpha = 0.006$), rupture velocities remain sub-Rayleigh. (middle and bottom) On a rougher fault ($\alpha = 0.008$ and 0.01), supershear velocities begin to appear, particularly at higher background stress levels.

fault geometries, at the same background shear stress $\tau_0 = 53.5$ MPa. The rupture patterns are remarkably complicated. Both ruptures start in the supershear regime, but then either transition back into the sub-Rayleigh regime or jump several kilometers to rerupture farther on the fault profile. Reruptures are often associated by the emission of both supershear and sub-Rayleigh slip pulses. An observer at $x = 5$ km on the left profile would see successively a supershear pulse at $t \approx 1$ s, its accompanying sub-Rayleigh rupture at $t \approx 2$ s, and a second supershear rupture coming from the opposite direction at $t \approx 5.5$ s. Although these highly complex rupture styles are unlikely to be common, our simulations suggest that they are possible. As discussed in the next section, there is emerging evidence for a broad diversity of rupture patterns in nature.

## 4. Quantitative Analysis of Supershear Ruptures

Having established that roughness favors complex rupture styles, we now focus our attention on the occurrence of supershear ruptures. We first examine the ensemble database in a statistical manner, by simply quantifying the overall prevalence of different rupture velocities, recorded at each ruptured grid point in all simulations, as a function of roughness and background stress. Figure 6 displays the obtained distributions for each roughness $\alpha$ and background shear stress $\tau_0$. We find that supershear rupture speeds become increasingly more likely on rougher faults. For the smoothest faults ($\alpha = 0.006$ and lower, not displayed here), the velocity distribution is concentrated in the region below the Rayleigh wave speed $c_R$. When $\alpha = 0.008$, for low

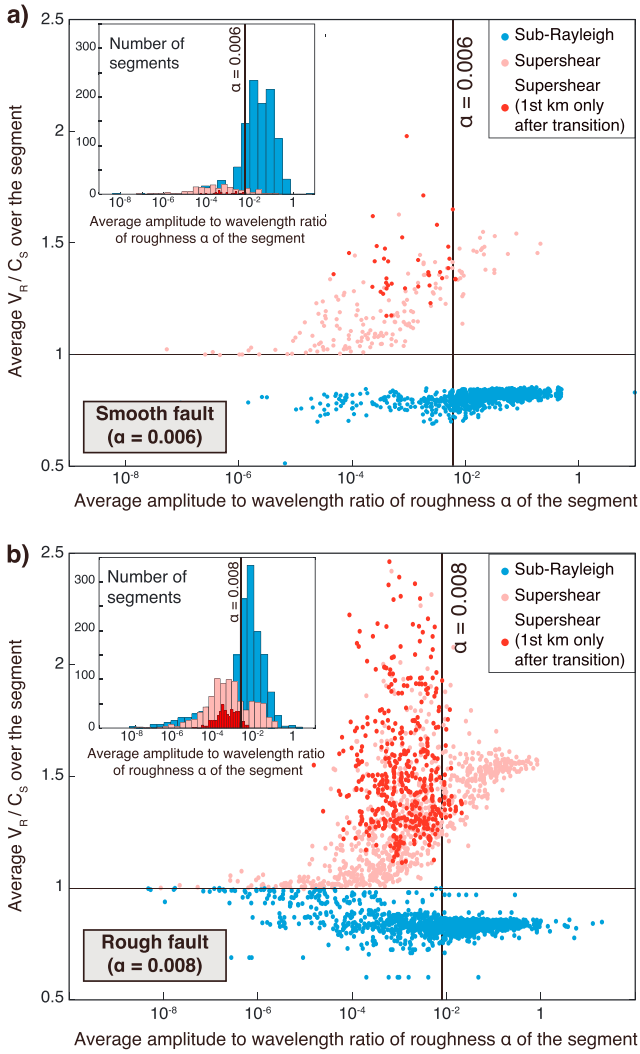


**Figure 7.** Relation between local rupture velocity and local amplitude-to-wavelength ratio of roughness $\alpha$, averaged over individual supershear (red) and sub-Rayleigh (blue) rupture segments. Smoother segments favor supershear propagation, especially immediately after the supershear transition (dark red). Insets show histograms of $\alpha$ for sub-Rayleigh and supershear segments. Results are shown for two levels of overall roughness: (a) $\alpha = 0.006$ and (b) $\alpha = 0.008$.

background shear stress, the rupture velocities remain in the sub-Rayleigh regime. Starting at $\tau_0 = 43.5$ MPa, a part of the distribution lies in the supershear region between the *S* wave speed $c_S$ and the *P* wave speed $c_P$. When $\tau_0$ increases, the fraction becomes larger. This shift toward supershear is accentuated for rougher faults ($\alpha = 0.01$). Consequently, the fraction of supershear rupture increases with both the initial background shear stress $\tau_0$ and the roughness $\alpha$. The increasing likelihood of supershear transients at larger $\tau_0$ supports the results of *Mena et al.* [2012] that supershear ruptures prevail in dynamic simulations with longer rupture length, which occurs more commonly in our simulations at larger background shear stresses. Also worth noticing is that the peak in the supershear velocity distribution is at approximately $0.9c_P$.

At face value, these results appear to be in contradiction to the prevailing view that smoother faults are most likely to host supershear events [*Bouchon et al.*, 2010]. However, this global analysis does not account for variations in the local roughness of the fault and the possible relation between local roughness and local rupture speeds. Nor does it distinguish highly localized supershear transients from sustained supershear propagation over long fault segments. Figure 7 addresses this issue. For two roughness levels $\alpha = 0.006$ and $\alpha = 0.008$, we isolate all sub-Rayleigh and supershear segments (of any length), then compute the average $\alpha$ and the average rupture velocity of each segment. The relation between roughness $\alpha$ and rupture velocity on individual

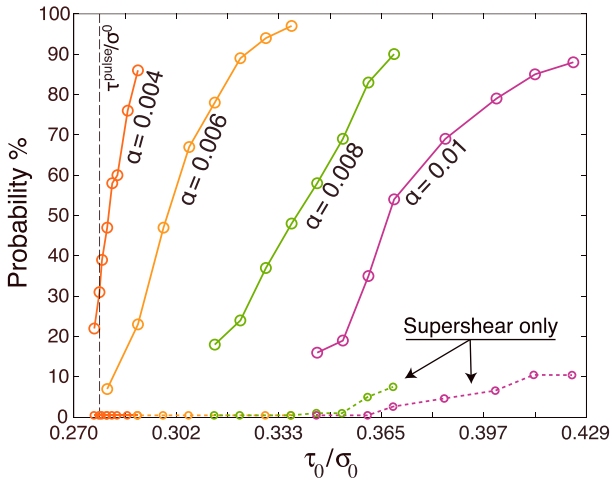


**Figure 8.** Percentage of ruptures reaching 20 km in either direction as a function of the ratio of background shear stress $\tau_0$ to effective normal stress $\sigma_0$, modified from Figure 6 in *Fang and Dunham* [2013]. Supershear ruptures are indicated in dotted lines. Higher stresses are necessary for a rupture to propagate the same distance on rougher faults. For a given shear stress, one may then estimate the chances of having a supershear rupture exceeding 20 km.

segments is shown in Figure 7, with the inset showing histograms of local roughness for sub-Rayleigh and supershear ruptures. Supershear segments tend to have smaller local roughness than sub-Rayleigh segments. This is especially true for the first kilometer of propagation after the supershear transition.

The results shown in Figures 6 and 7 lead us to conclude that increased geometric complexity at high $\alpha$ initiates many supershear transients, but stable propagation at supershear speeds is favored when subsequent sections of the fault are smoother.

Another method to study the ruptures is to classify them based on their rupture velocity and spatial extent and quantify the conditions that lead to large, supershear ruptures. For each rupture, we store the following two characteristics: the presence of supershear and the overall rupture length. Figure 8 displays the percentage of all ruptures and supershear ruptures only, exceeding 20 km, as a function of the background stress ratio $\tau_0/\sigma_0$ and the roughness $\alpha$. As explained before, a planar fault becomes capable of hosting self-sustaining slip pulses at a unique value of background shear stress close to $\tau^{\text{pulse}}$ [*Zheng and Rice*, 1998]. For faults of roughness $\alpha$, there is a distribution of possible lengths for a given background shear stress $\tau_0$ due to the stochastic variability in the fault geometry. For the smoothest faults, $\alpha = 0.004$ and 0.006, no supershear ruptures exceed 20 km at the range of stresses examined. Large supershear ruptures occur when $\alpha$ is large and their percentage increases with $\tau_0$. Therefore, only the roughest faults ($\alpha$ = 0.008 and 0.01) at elevated background shear stresses exhibit long supershear ruptures.

We compare these last results to the statistical analysis made by *Fang and Dunham* [2013] for the entire rupture catalog, as displayed in Figure 8. This approach can help quantify the range of stress levels, here indicated by $\tau_0/\sigma_0$, at which faults are likely to host large earthquakes. For a given fault roughness $\alpha$ and background shear stress $\tau_0$, we determine the probability for a rupture to reach a certain extent (solid line) and to be supershear as well (dashed line). This would be the probability of having an earthquake (supershear or not) on a fault of known roughness $\alpha$ given a nucleation event at the background stress $\tau_0/\sigma_0$. As tectonic loading gradually increases, nucleation events would constantly occur, driving ruptures outward along the fault. Most would arrest quickly but some would grow to become large earthquakes. The largest, system-spanning events would then relax stresses over the entire fault. This leads to fault operation in the range of stresses at which system-spanning events are capable of occurring. As Figure 8 shows, this range of stresses can be fairly broad, particularly for the rougher faults. Earthquakes at high $\tau_0/\sigma_0$, like the highly complex examples shown in Figure 5, will be uncommon, but are still expected to occur as extreme events. Similarly, examination of Figure 6 shows that for rougher faults, the range of stresses over which ruptures become supershear coincides with the range of stresses that the fault is expected to operate at.

| τ0 (MPa) | 1 | 2 | 3 | 4 | 5 | 6 | 7 | 8 | 9 | 10 | 11 | 12 | 13 | 14 | 15 | 16 | 17 | 18 | 19 | 20 | 21 | 22 | 23 | 24 | 25 |
|---|---|---|---|---|---|---|---|---|---|---|---|---|---|---|---|---|---|---|---|---|---|---|---|---|---|
| 36.5 | | | | | | | | | | | | | | | | | | | | | | | | | |
| 37.5 | | | | | | | | | | | | | | | | | | | | | | | | | |
| 38.5 | | | | | | | | | | | | | | | | | | | | | | | | | |
| 41.5 | | | | | ■ | | | | | | ■ | | | | ■ | | | | | | | | | ■ | |
| 42.5 | ■ | | | ■ | ■ | | | | | | ■ | | | | | | | | | | | ■ | ■ | ■ | |

| τ0 (MPa) | 26 | 27 | 28 | 29 | 30 | 31 | 32 | 33 | 34 | 35 | 36 | 37 | 38 | 39 | 40 | 41 | 42 | 43 | 44 | 45 | 46 | 47 | 48 | 49 | 50 |
|---|---|---|---|---|---|---|---|---|---|---|---|---|---|---|---|---|---|---|---|---|---|---|---|---|---|
| 36.5 | | | | | | | | | | | | | | | | | | | | | | | | | |
| 37.5 | | | | | | | | | ■ | | | | | | | | | | | | | | | | |
| 38.5 | | | | | | | | | | | | | ■ | | | | | | | | | | | | |
| 41.5 | | ■ | | | | | | | | | | | | | | ■ | | ■ | | | | | | | |
| 42.5 | | ■ | | | | | | | | | | | | | | ■ | | ■ | | | | | | | |

| τ0 (MPa) | 51 | 52 | 53 | 54 | 55 | 56 | 57 | 58 | 59 | 60 | 61 | 62 | 63 | 64 | 65 | 66 | 67 | 68 | 69 | 70 | 71 | 72 | 73 | 74 | 75 |
|---|---|---|---|---|---|---|---|---|---|---|---|---|---|---|---|---|---|---|---|---|---|---|---|---|---|
| 36.5 | | | | | | | | | | | | | | | | | | | | | | ■ | | | |
| 37.5 | | | | | | | | | | | | | | | | | | | | | | | | | |
| 38.5 | | | | | | | | | | | | | | | | | | | | | | | | | |
| 41.5 | | | | | ■ | ■ | | | | | | | | | | | | | | ■ | ■ | | | | |
| 42.5 | | | | | ■ | ■ | | | | | | | | | | | | | | ■ | ■ | | | | |

| τ0 (MPa) | 76 | 77 | 78 | 79 | 80 | 81 | 82 | 83 | 84 | 85 | 86 | 87 | 88 | 89 | 90 | 91 | 92 | 93 | 94 | 95 | 96 | 97 | 98 | 99 | 100 |
|---|---|---|---|---|---|---|---|---|---|---|---|---|---|---|---|---|---|---|---|---|---|---|---|---|---|
| 36.5 | | | | | | | | | | | | | | | | | | | | | | | | ■ | |
| 37.5 | | | | | ■ | | | | | | | ■ | | | | | | | | | | | | | |
| 38.5 | | | | | ■ | | | | | | | | | | | | | | | | | | | | |
| 41.5 | | | | | ■ | | ■ | | | | | | | | | | | | | | | | ■ | | |
| 42.5 | | | | | ■ | | | | | | ■ | | | | | | ■ | | | | | | ■ | | |

**Figure 9.** Table summarizing the occurrence of well-defined supershear ruptures (at least 1.5 km long) for medium roughness $\alpha = 0.006$ at different background shear stress $\tau_0$. Colored cells indicate cases with supershear. In most cases, supershear ruptures are more likely for larger values of $\tau_0$ and persist as $\tau_0$ increases. However, some transitions occur only in a narrow range of $\tau_0$ and cease at higher $\tau_0$.

## 5. Supershear Transition Mechanisms

We now describe several recurrent patterns for the supershear transition. We use the catalog for the medium roughness $\alpha = 0.006$, where supershear transitions start to appear and, unlike the examples in Figure 5, are not too complicated to analyze. Figure 9 documents the occurrence of well-defined supershear transitions of every fault profile and background shear stress used for this roughness. Each colored notch corresponds to

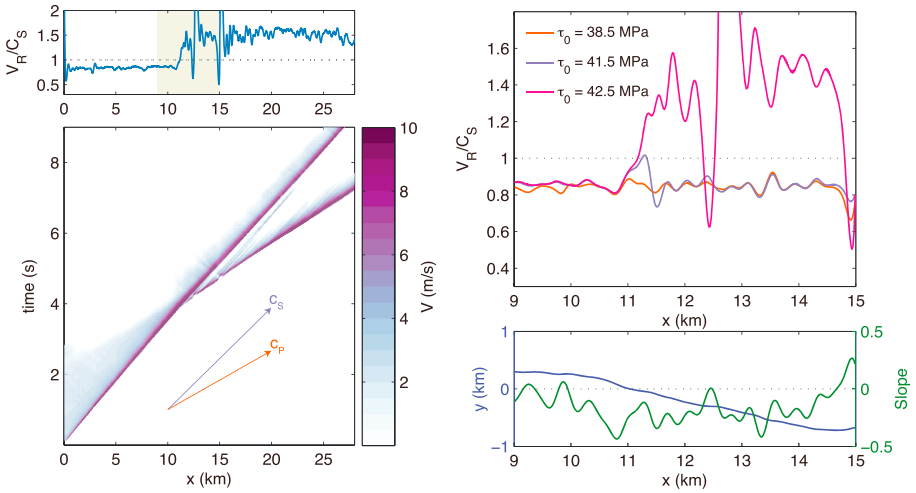


**Figure 10.** Supershear transition on a favorably oriented fault segment (releasing bend). Example is profile #23 with $\alpha = 0.006$. (bottom left) Space-time plot of slip velocity, showing rupture becoming supershear 11.5 km to the right of the hypocenter. (top left) Rupture velocity at the highest background stress with (top right) zoom-in around the transition location. (bottom right) Fault profile and slope around the bend.

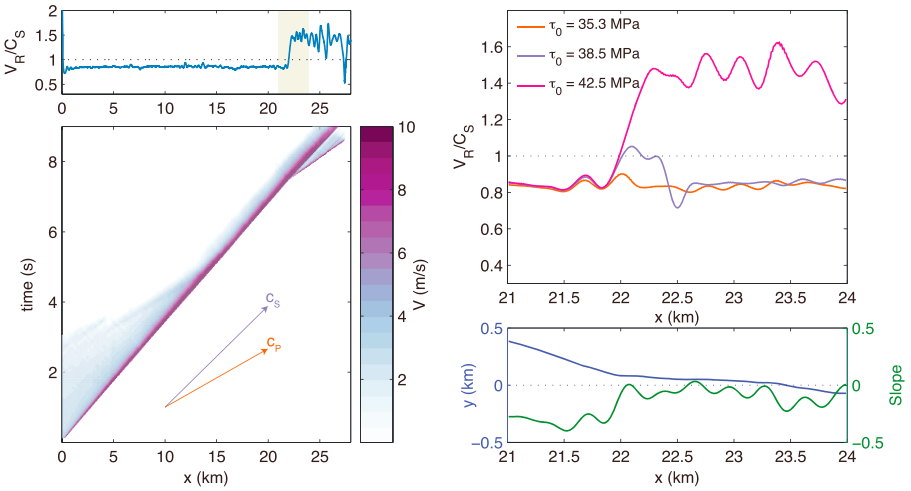


**Figure 11.** Supershear transient occurring on an unfavorably oriented fault segment. Example is profile #70 with $\alpha = 0.006$. (bottom left) Space-time plot of slip velocity, showing rupture becoming supershear 22 km to the right of the hypocenter. (top left) Rupture velocity at the highest background stress with (top right) zoom-in around the transition location. (bottom right) Fault profile and slope around the bend.

an event with a supershear transition. As seen previously, there is practically no supershear transition for the lowest background shear stress $\tau_0 = 36.5$ MPa (only 2/100 profiles). Upon increasing the background stress, the number of supershear ruptures increases (18/100 for $\tau_0 = 42.5$ MPa).

However, Figure 9 reveals something else. While most supershear transitions persist as $\tau_0$ continues to increase (e.g., profile #80), there are several cases in which the transition occurs only within a narrow range of $\tau_0$ (e.g., profile #34 or #87). We return to these cases below to better understand why the transition vanishes at higher stresses.

Three general patterns for the supershear transition emerge from the catalog study. The first one can be seen for fault profile #23 (Figure 10). The transition happens in a region where the slope is negative so the fault

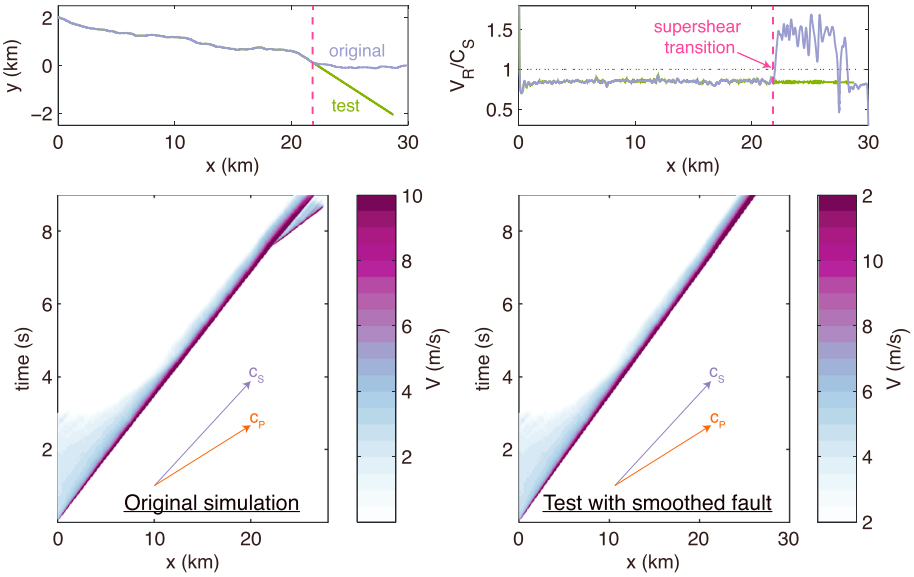


**Figure 12.** Test to confirm that the fault bend into a less favorable orientation is necessary to trigger supershear on the fault profile #70 (see also Figure 11). (bottom left) Space-time plot of slip velocity from the original simulation, showing rupture becoming supershear 22 km to the right of the hypocenter. (bottom left) Space-time plot of slip velocity for a fault that is planar after $x = 22$ km. (top left) Fault profiles. (top right) Rupture velocity. The rupture does not transition to supershear without the unfavorable bend.

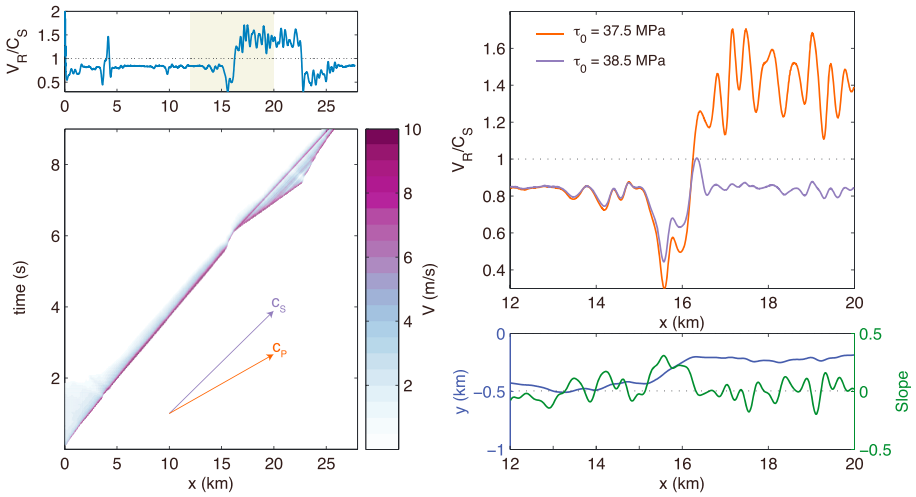


**Figure 13.** Example of a supershear transient triggered by a local restraining bend. Example is profile #87 with $\alpha = 0.006$. (bottom left) Space-time plot of slip velocity, showing rupture becoming supershear 16.5 km to the right of the hypocenter. (top left) Rupture velocity at two background stresses with (top right) zoom-in around the transition location. (bottom right) Fault profile and slope around the bend. At $\tau_0 = 37.5$ MPa, the bend temporarily delays the rupture, building a stress concentration and storing strain energy in the surrounding medium. Upon breaking through, the rupture jumps to a supershear speed. At a slightly higher stress, $\tau_0 = 38.5$ MPa, the deceleration is less pronounced and the transition does not occur.

has high resolved shear to effective normal prestress (i.e., a releasing bend). For the lowest background shear stress, the sub-Rayleigh rupture propagates smoothly. However, as the background shear stress increases, the rupture velocity around $x = 11$ km gradually rises, until it transitions to supershear at $\tau_0 = 42.5$ MPa. In contrast to some examples shown below, the supershear transition in this case is not initiated by any distinct geometrical feature at the transition location.

The second pattern is illustrated for fault profile #70 (Figure 11). The transition here occurs at a kink between a favorably oriented segment and a less, but still favorably oriented one. Before the transition, the slope of the fault profile is negative. In contrast to the results of *Dunham et al.* [2011b] for maximum compression angle $\Psi = 50°$, rupture velocity is positively correlated with fault slope. Pseudo-dynamic rupture models, like the one developed by *Trugman and Dunham* [2014], are based on the anticorrelation between slope and rupture velocity that characterizes sub-Rayleigh ruptures. It is clear that extending the pseudo-dynamic models to the supershear regime will require a closer examination of these exceptional cases. While the rupture velocity is insensitive to the background stress before the bend, the rupture becomes highly sensitive to the local fault geometry as it traverses the bend. Similar to the previous example, the supershear transition occurs as the background shear stress increases. To confirm the key role played by the bend toward a less favorable orientation, we perform another simulation in which the bend was removed by prolonging the fault geometry with the same slope after $x = 22$ km (Figure 12). The supershear transition does not happen with the modified geometry.

The two patterns described above are characterized by robust supershear transitions that persist with increasing background shear stress. The last case we present (fault profile #87, Figure 13) illustrates a transition that occurs only within a narrow range of stress. In this case, the transition occurs at a small restraining bend. As the rupture enters the bend, it decelerates and nearly arrests. This builds a local stress concentration and stores strain energy in the surrounding medium. When the rupture breaks through the bend, it taps this energy and impulsively surges forward at a supershear speed. Supershear speeds are sustained for a while due to the favorable orientation of the following segment. When the background stress is increased, the small bend is insufficient to delay the rupture enough for this slingshot effect to occur, and the rupture remains sub-Rayleigh. In many ways, this transition mechanism is similar to the one identified by *Dunham et al.* [2003] in 3-D simulations of ruptures on planar faults that encounter local stress or strength heterogeneities.

## 6. Conclusions

In this study, we examined a collection of over a thousand plane strain dynamic ruptures in 2-D on different realizations of fractally rough faults originally compiled in *Fang and Dunham* [2013]. We first showed that roughness favors extremely diverse rupture styles, such as reverse ruptures, secondary pulses, and supershear transitions. We then demonstrated, through a statistical analysis of the prevalence of supershear transients, that supershear transitions become increasingly more likely on rougher faults. However, sustained supershear propagation tends to occur on sections of the fault that are smoother than average. Finally, we investigated specific cases of supershear ruptures, showing that the supershear transition can be associated with propagation into an unfavorably oriented segment or initiated by temporary deceleration at a local unfavorable bend.

Our study is broadly consistent with the field observations [*Bouchon et al.*, 2010] that indicate that smoother, geometrically simple fault segments are most favorable for supershear propagation. Smooth faults are undoubtedly conducive to sustained supershear propagation because radiative energy losses from rupture acceleration and deceleration are minimized, leading to a higher energy release rate at the same average rupture velocity than ruptures on rougher faults. Yet our work points out that in many cases, a short unfavorable segment might allow the transient development of high stresses that can then drive the rupture from sub-Rayleigh to supershear speeds. This is especially necessary if faults indeed operate at the low background stress levels suggested by recent work on dynamic weakening, so that the classic Burridge-Andrews transition mechanism cannot occur. However, these geometric complexities can be very small and might go unnoticed or simply not be expressed in the surface trace of a fault.

The connection between rupture velocity and fault geometry naturally leads to the question of whether studies of fault geometry, as directly measured at the surface or inferred from seismicity at depth, might lead to predictions of locations where supershear propagation, or other complex rupture styles, is expected. Unfortunately, for each geometric feature that is associated with a supershear transition, there are many nearly identical geometric features through which ruptures propagate at sub-Rayleigh speeds. Furthermore, we also find that some geometric features causing supershear only do so for a specific range of stresses, and it would likely be impossible to measure and monitor stress at seismogenic depths with the resolution required for accurate predictions of rupture velocity.

This high degree of sensitivity and nonlinearity extends to other aspects of rupture propagation on rough faults, such as rupture arrest and the occurrence of secondary or even multiple slip pulses. It follows that deterministic predictions of rupture behavior from fault geometry are unlikely to be successful. In contrast, statistical characterizations that acknowledge and incorporate the stochastic nature of the rupture process appear far more promising. The ensemble dynamic rupture approach seems well suited for this endeavor, as illustrated with the construction of a pseudo-dynamic model by *Trugman and Dunham* [2014] based on the correlation between kinematic source parameters and local fault slope. Their analysis was restricted to sub-Rayleigh slip pulses but possibly could be extended to include the much broader range of rupture styles and speeds that we have documented in this study.

An unsettling result of our investigation is the occurrence of extreme events, like those shown in Figure 5, featuring values of slip far above those typically observed on faults of this size and multiple slip pulses that are simultaneously active on the fault. While these ruptures require very high background stress levels, the statistical analysis in Figure 8 suggests that these stress levels might occasionally arise, albeit infrequently, on natural faults.

**Acknowledgments**
This work was supported by the National Science Foundation (ACI-1148493) and the Southern California Earthquake Center. SCEC is funded by NSF Cooperative agreement EAR-1033462 and USGS Cooperative agreement G12AC20038. The SCEC contribution number for this paper is 6052. No data were used in this study. Simulations were done using the finite difference code FDMAP, available at https://pangea.stanford.edu/edunham/codes/codes.html. Input files to reproduce simulation results are available upon request. We thank the Associate Editor and the two anonymous reviewers for their insightful comments.

## References

Aagaard, B. T., and T. H. Heaton (2004), Near-source ground motions from simulations of sustained intersonic and supersonic fault ruptures, *Bull. Seismol. Soc. Am.*, *94*(6), 2064–2078, doi:10.1785/0120030249.

Andrews, D. J. (1976), Rupture velocity of plane strain shear cracks, *J. Geophys. Res.*, *81*(32), 5679–5687, doi:10.1029/JB081i032p05679.

Andrews, D. J. (1980), A stochastic fault model: 1. Static case, *J. Geophys. Res.*, *85*(B7), 3867–3877, doi:10.1029/JB085iB07p03867.

Andrews, D. J. (1985), Dynamic plane-strain shear rupture with a slip-weakening friction law calculated by a boundary integral method, *Bull. Seismol. Soc. Am.*, *75*(1), 1–21.

Archuleta, R. J. (1984), A faulting model for the 1979 Imperial Valley earthquake, *J. Geophys. Res.*, *89*(B6), 4559–4585, doi:10.1029/JB089iB06p04559.

Beroza, G. C., and P. Spudich (1988), Linearized inversion for fault rupture behavior: Application to the 1984 Morgan Hill, California, earthquake, *J. Geophys. Res.*, *93*(B6), 2156–2202, doi:10.1029/JB093iB06p06275.

Bouchon, M., and M. Vallée (2003), Observation of long supershear rupture during the magnitude 8.1 Kunlunshan earthquake, *Science*, *301*(5634), 824–826, doi:10.1126/science.1086832.
Bouchon, M., N. Toksöz, H. Karabulut, M. P. Bouin, M. Dietrich, M. Aktar, and M. Edie (2000), Seismic imaging of the 1999 Izmit (Turkey) rupture inferred from the near-fault recordings, *Geophys. Res. Lett.*, *27*(18), 3013–3016, doi:10.1029/2000GL011761.
Bouchon, M., M. P. Bouin, H. Karabulut, M. Nafi Toksöz, M. Dietrich, and A. J. Rosakis (2001), How fast is rupture during an earthquake? New insights from the 1999 Turkey earthquakes, *Geophys. Res. Lett.*, *28*(14), 2723–2726, doi:10.1029/2001GL013112.
Bouchon, M., H. Karabulut, M. P. Bouin, J. Schmittbuhl, M. Vallée, R. Archuleta, S. Das, F. Renard, and D. Marsan (2010), Faulting characteristics of supershear earthquakes, *Tectonophysics*, *493*(3–4), 244–253, doi:10.1016/j.tecto.2010.06.011.
Brodsky, E. E., J. J. Gilchrist, A. Sagy, and C. Collettini (2011), Faults smooth gradually as a function of slip, *Earth Planet. Sci. Lett.*, *302*(1–2), 185–193, doi:10.1016/j.epsl.2010.12.010.
Brown, S. R., and C. H. Scholz (1985), Broad bandwidth study of the topography of natural rock surfaces, *J. Geophys. Res.*, *90*(B14), 12,575–12,582, doi:10.1029/JB090iB14p12575.
Burridge, R. (1973), Admissible speeds for plane-strain self-similar shear cracks with friction but lacking cohesion, *Geophys. J. R. Astron. Soc.*, *35*(4), 439–455, doi:10.1111/j.1365-246X.1973.tb00608.x.
Candela, T., F. Renard, M. Bouchon, A. Brouste, D. Marsan, J. Schmittbuhl, and C. Voisin (2009), Characterization of fault roughness at various scales: Implications of three-dimensional high resolution topography measurements, *Pure Appl. Geophys.*, *166*(10–11), 1817–1851, doi:10.1007/s00024-009-0521-2.
Candela, T., F. Renard, Y. Klinger, K. Mair, J. Schmittbuhl, and E. E. Brodsky (2012), Roughness of fault surfaces over nine decades of length scales, *J. Geophys. Res.*, *117*, B08409, doi:10.1029/2011JB009041.
Chester, F. M., and J. S. Chester (2000), Stress and deformation along wavy frictional faults, *J. Geophys. Res.*, *105*(B10), 23,421–23,430, doi:10.1029/2000JB900241.
Das, S., and K. Aki (1977), A numerical study of two-dimensional spontaneous rupture propagation, *Geophys. J. R. Astron. Soc.*, *50*, 643–668, doi:10.1111/j.1365-246X.1977.tb01339.x.
Di Toro, G., D. L. Goldsby, and T. E. Tullis (2004), Friction falls towards zero in quartz rock as slip velocity approaches seismic rates, *Nature*, *427*(6973), 436–439, doi:10.1038/nature02249.
Dieterich, J. H., and D. E. Smith (2009), Nonplanar faults: Mechanics of slip and off-fault damage, *Pure Appl. Geophys.*, *166*(10–11), 1799–1815, doi:10.1007/s00024-009-0517-y.
Dunham, E. M. (2007), Conditions governing the occurrence of supershear ruptures under slip-weakening friction, *J. Geophys. Res.*, *112*, B07302, doi:10.1029/2006JB004717.
Dunham, E. M., and R. J. Archuleta (2004), Evidence for a supershear transient during the 2002 Denali fault earthquake, *Bull. Seismol. Soc. Am.*, *94*(6B), S256–S268, doi:10.1785/0120040616.
Dunham, E. M., P. Favreau, and J. M. Carlson (2003), A supershear transition mechanism for cracks, *Science*, *299*(5612), 1557–1559.
Dunham, E. M., D. Belanger, L. Cong, and J. E. Kozdon (2011a), Earthquake ruptures with strongly rate-weakening friction and off-fault plasticity, Part 1: Planar faults, *Bull. Seismol. Soc. Am.*, *101*(5), 2296–2307, doi:10.1785/0120100075.
Dunham, E. M., D. Belanger, L. Cong, and J. E. Kozdon (2011b), Earthquake ruptures with strongly rate-weakening friction and off-fault plasticity, Part 2: Nonplanar faults, *Bull. Seismol. Soc. Am.*, *101*(5), 2308–2322, doi:10.1785/0120100076.
Ellsworth, W. L., and M. Celebi (1999), Near field displacement time histories of the *M* 7.4 Kocaeli (Izmit), Turkey, earthquake of August 17, 1999, *EOS Trans. AGU*, *80*(46), F648, Fall Meet. Suppl., Abstract #F648.
Ellsworth, W. L., M. Celebi, J. R. Evans, E. G. Jensen, R. Kayen, M. C. Metz, D. J. Nyman, J. W. Roddick, P. Spudich, and C. D. Stephens (2004), Near-field ground motion of the 2002 Denali fault, Alaska, earthquake recorded at pump station 10, *Earthquake Spectra*, *20*(3), 597–615, doi:10.1193/1.1778172.
Fang, Z., and E. M. Dunham (2013), Additional shear resistance from fault roughness and stress levels on geometrically complex faults, *J. Geophys. Res. Solid Earth*, *118*, 3642–3654, doi:10.1002/jgrb.50262.
Gabriel, A.-A., J.-P. Ampuero, L. A. Dalguer, and P. M. Mai (2012), The transition of dynamic rupture styles in elastic media under velocity-weakening friction, *J. Geophys. Res.*, *117*, B09311, doi:10.1029/2012JB009468.
Haskell, N. (1964), Total energy and energy spectral density of elastic wave radiation from propagating faults, *Bull. Seismol. Soc. Am.*, *54*(6), 1811–1841.
Heaton, T. (1982), The 1971 San Fernando earthquake: A double event?, *Bull. Seismol. Soc. Am.*, *72*(6), 2037–2062.
Heaton, T. H. (1990), Evidence for and implications of self-healing pulses of slip in earthquake rupture, *Phys. Earth Planet. Inter.*, *64*(1), 1–20, doi:10.1016/0031-9201(90)90002-F.
Kaneko, Y., and N. Lapusta (2010), Supershear transition due to a free surface in 3-D simulations of spontaneous dynamic rupture on vertical strike-slip faults, *Tectonophysics*, *493*(3–4), 272–284, doi:10.1016/j.tecto.2010.06.015.
Kozdon, J. E., E. M. Dunham, and J. Nordström (2012), Interaction of waves with frictional interfaces using summation-by-parts difference operators: Weak enforcement of nonlinear boundary conditions, *J. Sci. Comput.*, *50*(2), 341–367, doi:10.1007/s10915-011-9485-3.
Kozdon, J. E., E. M. Dunham, and J. Nordström (2013), Simulation of dynamic earthquake ruptures in complex geometries using high-order finite difference methods, *J. Sci. Comput.*, *55*(1), 92–124, doi:10.1007/s10915-012-9624-5.
Lee, J. J., and R. L. Bruhn (1996), Structural anisotropy of normal fault surfaces, *J. Struct. Geol.*, *18*(8), 1043–1058, doi:10.1016/0191-8141(96)00022-3.
Liu, Y., and N. Lapusta (2008), Transition of mode II cracks from sub-Rayleigh to intersonic speeds in the presence of favorable heterogeneity, *J. Mech. Phys. Solids*, *56*(1), 25–50, doi:10.1016/j.jmps.2007.06.005.
Mena, B., L. A. Dalguer, and P. M. Mai (2012), Pseudodynamic source characterization for strike-slip faulting including stress heterogeneity and super-shear ruptures, *Bull. Seismol. Soc. Am.*, *102*(4), 1654–1680, doi:10.1785/0120110111.
Meng, L., J. P. Ampuero, M. T. Page, and K. W. Hudnut (2011), Seismological evidence and dynamic model of reverse rupture propagation during the 2010 *M*7.2 El Mayor Cucapah earthquake, Abstract S52B-04 presented at 2011 Fall Meeting, AGU, San Francisco, Calif., 5–9 Dec.
Noda, H., E. M. Dunham, and J. R. Rice (2009), Earthquake ruptures with thermal weakening and the operation of major faults at low overall stress levels, *J. Geophys. Res.*, *114*, B07302, doi:10.1029/2008JB006143.
Power, W. L., and T. E. Tullis (1991), Euclidean and fractal models for the description of rock surface roughness, *J. Geophys. Res.*, *96*(B1), 415–424, doi:10.1029/90JB02107.
Power, W. L., and T. E. Tullis (1995), A review of the fractal character of natural fault surfaces with implications for friction and the evolution of fault zones, in *Fractals in the Earth Sciences*, pp. 89–105, Springer, New York.
Power, W. L., T. E. Tullis, and J. D. Weeks (1988), Roughness and wear during brittle faulting, *J. Geophys. Res.*, *93*(B12), 15,268–15,278, doi:10.1029/JB093iB12p15268.

Robinson, D. P., C. Brough, and S. Das (2006), The $M_w$ 7.8, 2001 Kunlunshan earthquake: Extreme rupture speed variability and effect of fault geometry, *J. Geophys. Res.*, *111*, B08303, doi:10.1029/2005JB004137.

Sagy, A., and E. E. Brodsky (2009), Geometric and rheological asperities in an exposed fault zone, *J. Geophys. Res.*, *114*, B02301, doi:10.1029/2008JB005701.

Shi, Z., and S. M. Day (2013), Rupture dynamics and ground motion from 3-D rough-fault simulations, *J. Geophys. Res. Solid Earth*, *118*, 1122–1141, doi:10.1002/jgrb.50094.

Spudich, P., and L. Frazer (1984), Use of ray theory to calculate high-frequency radiation from earthquake sources having spatially variable rupture velocity and stress drop, *Bull. Seismol. Soc. Am.*, *74*(6), 2061–2082.

Trugman, D. T., and E. M. Dunham (2014), A 2-D pseudodynamic rupture model generator for earthquakes on geometrically complex faults, *Bull. Seismol. Soc. Am.*, *104*(1), 95–112, doi:10.1785/0120130138.

Tsutsumi, A., and T. Shimamoto (1997), High-velocity frictional properties of gabbro, *Geophys. Res. Lett.*, *24*(6), 699–702, doi:10.1029/97GL00503.

Tullis, T. E., and D. L. Goldsby (2003), Flash melting of crustal rocks at almost seismic slip rates, *Eos Trans. AGU*, *84*(46), Fall Meet. Suppl., Abstract S51B–05.

Vallée, M., M. Landès, N. M. Shapiro, and Y. Klinger (2008), The 14 November 2001 Kokoxili (Tibet) earthquake: High-frequency seismic radiation originating from the transitions between sub-Rayleigh and supershear rupture velocity regimes, *J. Geophys. Res.*, *113*, B07305, doi:10.1029/2007JB005520.

Wald, D. J., and P. G. Somerville (1995), Variable-slip rupture model of the great 1923 Kanto, Japan, earthquake—Geodetic and body-waveform analysis, *Bull. Seismol. Soc. Am.*, *85*(1), 159–177.

Yue, H., T. Lay, J. T. Freymueller, K. Ding, L. Rivera, N. A. Ruppert, and K. D. Koper (2013), Supershear rupture of the 5 January 2013 Craig, Alaska ($M_w$ 7.5) earthquake, *J. Geophys. Res. Solid Earth*, *118*, 5903–5919, doi:10.1002/2013JB010594.

Zheng, G., and J. R. Rice (1998), Conditions under which velocity-weakening friction allows a self-healing versus a cracklike mode of rupture, *Bull. Seismol. Soc. Am.*, *88*(6), 1466–1483.